International Journal of Impact Engineering, Volume 35, Issue 5, May 2008, Pages 347-362

Application of the finite element method to predict the crashworthy response of a metallic helicopter under floor structure onto water

K.Hughes*, J.Campbell, R.Vignjevic

Crashworthiness, Impacts and Structural Mechanics Group,

School of Engineering, Cranfield University, Cranfield, BEDS, MK43 0AL, UK

www.cranfield.ac.uk/soe/structures

* - Corresponding author : Tel: +44 1234 750111 x5172

Email addresses:

k.hughes@cranfield.ac.uk; j.campbell@cranfield.ac.uk, v.rade@cranfield.ac.uk

Abstract

Helicopters are seen by the petroleum industry as the only viable way of transportation between on and offshore platforms. At present, there exists no certification requirement to ensure a high level of survivability in the event of a water impact. Within the literature, there exists a body of information related to the post crash analysis of accident data, which supports the finding that a conventional metallic under floor design performs poorly during a water impact, in relation to the transmission of water pressure and the absorption of energy.

In order to characterise this behaviour, this paper concerns the crashworthiness of helicopters on water for an impact speed of $8ms^{-1}$, for a simple box-beam construction

that is comman to metallic helicopters. A complete section-by-section analysis of a component floor will be presented, which has been compared both quantatively and qualitatively with the results provided by the finite element code, LS-DYNA3D. Comparisons will be made to collapsed frame height, as well as to detailed measurements for skin deflection. The main areas of good and poor agreement are discussed and conclusions drawn on the validity of the simulations, with a view for developing a practical methodology for fluid-structure interactions.

This paper discusses the recommendations for design changes that could potential improve the level of crashworthiness currently offered, through the careful redesign of frames and joints, in order to allow for progressive collapse and sustained energy absorption. This paper concludes with a recommendation that a next generation design must incorporate a passive dual role capability that can cater for both hard and soft surface impacts, by being able to degrade its localised strength depending upon the type of surface encountered.

Keywords: Crashworthiness, helicopter, testing, water, failure, design

1. Introduction

The earliest recorded work that investigates the effects of a man made object impacting on water can be traced back to 1929, where Von Karman developed the first theoretical model to calculate the forces encountered during rigid seaplane floats impacting onto water [1]. This approach utilised the concept of added mass, which was a difficult

parameter to quantify, but provided a good starting point for developing understanding in this field, which was subsequently extended and adopted during later works.

In the early days of helicopter crashworthiness development, a small cross-section of experimental data was available. Typically, these were reviewed by separate agencies and the information was generally fragmented, making it difficult to identify potential design improvements, or amend current regulations.

This problem was first addressed in 1986 by providing a historical review of civil helicopter accidents occurring between 1974 and 1978, which was later followed by a review of US Navy and Army accidents in the same year [2, 3]. This was again reviewed in 1993 for helicopter ditchings onto water that occurred between 1982 and 1989. This was performed in two phases, where part I dealt with the analysis of the impact and post impact conditions [4], and part II provided an assessment of the structural response on occupant injury, the identification of ways of alleviating injury, together with an evaluation of current numerical techniques for modelling impacts onto water [5]. Several full-scale helicopter drop tests have also been performed in recent years in order to provide a greater understanding of the phenomena associated with fluid-structure interactions [6-9].

This research has identified that the water environment poses a unique design case, for which conventional designs perform poorly, in terms of transmitting the water pressure and the absorption of energy. The poor transmission of these loads, coupled with a high failure strength of the surrounding structure, means that frame collapse does not occur and high forces and accelerations are passed through the airframe. This in turn can lead to the distortion of the passenger floor and preventing the energy absorbing seats from

operating effectively, through to the jamming or loss of the doors. A more serious problem concerns loss in floatation capability if skin integrity fails and the resulting internal damage that will occur.

This paper concerns the crashworthiness of helicopters onto water and provides a complete section-by-section analysis of a representative sub floor section that was dropped as part of an EU project (*CAST,* whose aim was to develop simulation tools and a design methodology that will permit cost effective design and entry into service of crashworthy helicopters for impacts onto both ground and water [9].

This paper is split into two parts, with the first providing a description of the test facilities, the choice of boundary conditions and the instrumentation applied to the structure, and the second part will provide a detailed classification of the different failure modes observed. The assessment of the crashworthy response will enable limitations to be identified, which will have a profound impact on future metallic helicopter design and significantly improve occupant survivability during an impact on water.

2. Sub Floor Specimen

The component floor was manufactured from an aluminium 2014 alloy and taken from the aft part of the main passenger section of a WG30 helicopter, between STN1210A and 370A. This component had a mass of 41kg and was 2170mm wide, 970mm long and 163mm high, and its location relative to the airframe can be found in figure 1.

The sub floor is a lattice construction consisting of longitudinal and lateral frames manufactured from metallic sheets. The longitudinal frames are reinforced by three

evenly spaced L-section stiffeners and are attached to the upper seat track assemblies with a uniform rivet pitch of 25mm. The lower parts are reinforced with z-section stiffeners, which also provide a riveted attachment to the lower skin.

The frames orientated in the transverse direction are also manufactured from metallic sheet and are typically shorter in length. STN370A consists of a combination of single and double skinned metallic frames, to which L-section brackets are riveted to provide attachment points for the passenger floor. These transverse frames are connected to the longitudinal frames via C-section overlaps to form individual box-sections. The transverse frames contain a central cut out for a longitudinal z-section stringer that provides structural rigidity for the skin.

The curved end-sections are riveted directly to the main longitudinal end frames, which provide a direct load path for the main engine and gearbox assemblies to the impacted surface. STN1210A represent an extremely strong construction, as the port and starboard landing gear attachments form part of this frame. The passenger floor is attached via tapered screws and is manufactured from a composite material called Fibrelam, which consists of unidirectional glass fibres bonded to a honeycomb / aramid core. The outer skin is also manufactured from metallic sheets and riveted to all longitudinal and transverse frames. A summary of the main dimensions and component thicknesses can be found in tables 1 and 2 respectively.

3. Experimental drop test

The objective of the drop test was two-fold. Firstly, it would allow the identification of the global collapse and failure mechanisms of this design and secondly, to provide quantitative data to support and validate numerical modelling.

The test was performed at the CIRA Water Impact Facility in Italy, which consists of a 4m deep tank and an 11m high tower that enables guided descents [10]. The component floor was rigidly attached to the guided trolley assembly through 18 attachment rods connected directly to the seat rails [11]. This ensured the desired attitude of an $8ms^{-1}$ near-normal impact was obtained. Ballast was added through the attachment of lead plates as shown in figure 2, in order to take into account the load path of the passenger seats and occupants, together with the mass of the surrounding airframe. A mass breakdown can be found in table 3.

The data acquisition system collected data from 32 channels sampling at 10kHz, which provided measurements of the accelerations and pressures at various locations. In order to isolate the pressure transducers from the deformation of the panels, the sensors were mounted on square steel plates that had a cross section of 15x15mm and a thickness of 2mm. Bi-adhesive tape was then used to attach the sensors to the steel plate. All constituent parts of the data acquisition system were calibrated in order to conform to SAE/J211 and also included. The final part of this system was two Kodak high-speed digital cameras capable of capturing 1000 frames per second for one second, in order to provide a visual check of the impact conditions [12].

4. Finite element modelling

The drop test was recreated using LS-DYNA3D, where in order to determine its capability as a predictive tool for fluid-structure interactions. As no methodology exists for this type of analysis, this paper assumes the end-user is an engineer and not a developer of the code. Therefore, only basic definitions and default parameters were chosen, except in situations where the quality of the results dictated refinements were necessary. This would allow any short comings to be identified, as well as determining the dominant parameters that affect numerical accuracy.

The finite element model in figure 3 contains all principal components, stiffeners and load attachment points were modelled using an average element size of 30mm, resulting in 80,622 nodes, 61,516 shells, using an average element size of 3cm and 1,845 rivet definitions. The following is a summary of the main parameters, with the water being treated separately in section 4.1.

- All metallic components were manufactured from aluminium 2014 and represented by a tabulated linear piecewise material model, using the values in table 4. An element deletion criterion based upon a limiting plastic strain of 16% was also incorporated.
- The passenger floor was represented using *MAT_COMPOSITE_MATRIX, which determines the elastic response by calculating the force and momentum results from the membrane strains and shell curvatures from the laminate constitutive equation. This elastic assumption was necessary as accurate material data for Fibrelam was unavailable, and as the floor is not part of the main load path, this simplification would not affect the global structural response.

- The rivets were approximated by multi-layered rigid links, with an that are allowed to separate when the effective nodal plastic failure strain exceeds a limiting value of 10%. This can be used to model the tearing of a rivet from a component since the plasticity is based on the surrounding material and not the rivet itself. Brittle failure was not considered due to premature failure caused by force spikes during initial runs. Due to the varying element size, the global value assigned may underestimate / overestimate the strength of the rivets, but this can be refined during subsequent iterations.

- For all shells, the Belytschko-Wang-Chiang under integrated element formulation was assigned, which utilises two integration points through the thickness and a 2x2 gauss quadrature integration rule for the cross-section. All triangular elements were assigned a C_0 tria element formulation using default parameters.

- Different hour glassing control schemes were tried and it was found that the viscous based formulation using the default values was able to minimise these spurious modes in certain high deformation locations. In areas still exhibiting problems, upgrading to a fully integrated formulation is recommended, as will be discussed later.

- In order to represent the guided descent, lumped masses represented the ballast and trolley, where the nodes were constrained to move equivalently in the vertical direction only, with an initial velocity of $8ms^{-1}$.

- Acceleration time histories were obtained by allocating a 50g mass at the corresponding nodal locations. The pressure time histories were obtained from

the contact algorithm defined between the elements in the water and skin, where only the slave side (skin) was considered.

- An automatic single surface contact algorithm was globally assigned using a penalty stiffness factor of 0.3. Gravity was also incorporated.
- The simulations were performed on a four-processor Dec-Alpha machine with a UNIX version of LS-DYNA3D (V960). Mass scaling was not used, resulting in 130 CPU hours being required to simulate the first 35ms of impact, taking approximately 31 hours to complete.

4.1 Water modelling

LS-DYNA3D currently offers three different formulations for simulating fluid-structure interactions. The first is purely Lagrangian, where the water is represented by fixed mass elements, the second is to adopt an arbitrary-Lagrange-Eulerian (ALE) approach, where a deformable Lagrangian structure moves through an Eulerian mesh and finally, a Smooth Particle Hydrodynamic (SPH) option, which uses individual particles to represent a continuum. Each formulation has its own advtanages and disadvantages. For example, ALE and SPH overcome the stability issues associated with large deformations that generally limit the applicability of conventional Lagrangian finite elements, but introduces their own unique problems.

As this research was interested in captuting the structural deformation during the initial stages of a water impact, where the intertial forces dominate over viscous, a Lagrangian approach was deemed to be the most suitable. It is accepted that this may not represent

the dynamic impedance of test, as representing the layer of air between fluid and structure would not be possible. However, this limitation was deemed acceptable, as the approach can always be refined if an increase in numerical functionality is required.

In order to scope the size of the model, a separate numerical sensitivity analysis was performed, which involved comparing experimental acceleration time histories for rigid wooden shapes impacting onto water [13]. For an impactor size of 1m and an impact velocity ranging from 3 to 10ms^{-1}, the water component required a minimum depth of 1.2m and a lateral excess of 1m around the footprint of the impactor [14]. A baseline response was obtained using a uniform 5cm element size and a tuned penalty stiffness factor of 0.3.

To reduce the number of elements, in-plane element biasing was not used in order to minimise errors that may arise during wave transmission through varying mesh densities. The only remaining option was to vary the number of elements through thickness and compare results to the uniform baseline. The convergence of accelerations and the formation of the initial pressure wave were used as the stopping criteria, which led to the identification of a minimum number of ten layers being required, before the elements could be expanded by a factor of 1.25 until the desired depth was reached.

A polynomial equation of state was defined, together with non-reflecting boundary conditions assigned to the free surfaces. Using an 5cm element length, this led to the generation of 76K solid elements for a water component with dimensions (4.0x3.0x1.2)m. Fully integrated elements were needed in order to overcome the unrealistic response generated by under integrated elements in the form of clear sink lines located directly beneath the main frames.

$$P = C_0 + C_1\mu + C_2\mu^2 + C_3\mu^3 + \left(b_0 + b_1\mu + b_2\mu^2\right)E \quad ,$$

where C_i are the material constants, $\mu+1 = 1/V$ (where V is the relative volume) and E represents the internal energy. The following coefficients were used; $C_0 = 0$ GPa, $C_1 = 2.723$ GPa, $C_2 = 10.45$ GPa, $C_3 = 30.11$ GPa, and $(b_0 + b_1\mu + b_2\mu^2) = 0$ [15].

5. Main features of a water impact : Post test observations

The main features of damage and failure have been directly annotated onto figure 4, where the instrumentation cables and passenger floor have been removed for clarity. The longitudinal V830, V480 and V0 remain relatively undamaged, which is consistent with current understanding. The skin deflects in-between these frames with the peak deflection occurring at the mid points, which explains the localised material failure observed in STN370A shown in figure 5.

Only the port side could be considered for comparative purposes, as the numerical idealisation did not take into account the replacement skin panel that was added, or the removal of the port landing gear attachment shown in figure 6, which would affect the localised stiffness at these locations.

The skin panels located between the longitudinal frames are subject to large deformations, as ductile failure was observed in two limited areas between V480 and V830, which are highlighted as locations #1 and #2 in figure 4. However, the levels of damage are not symmetric, as it is more severe on the starboard side. Skin failure at location #2 can be discounted, as the test specimen was pre-damaged at this location, as a replacement skin panel was added, together with the removal of the port landing gear

attachment it is the consequence of the replaced panel. Despite the fact, this damage is not considered to be representative, this degree of failure still serves as a severe example of the damage that could be potentially experienced of the effects skin failure can have on the by the surrounding components.

The port skin separation (location #1) can be attributed to the substantial construction of the surrounding structure (port landing gear attachment), when compared to the flexible skin. As the skin deflects, the rivets are loaded in both shear and tension. Failure is in the form of simple pull out due to hole elongation in the skin, which propagates along both lateral and longitudinal rivet lines.

Limited deformation is observed along the curved end sections, as the structure in this location is substantially reinforced by the landing gear assemblies on one side and by reinforcing brackets on the other. The skin deflections that occur are relatively minor, due to the curvature of the skin that redirects the water surface, minimising the loading at these locations.

6. Overview of the numerical results

The predicted response 35ms after impact can be found in figure 7, where the passenger floor has been removed for clarity. There are several locations where numerical instabilities occur, which were caused in part by the expected mesh distortions along the boundary between fluid and structure, together with hourglassing modes in components subject to large deformations, such as the upper rail assemblies and frame stringers, which can completely change the resulting failure mode.

Different hour glassing control schemes were tried and it was found that a viscous based formulation coped well with minimsing this effect. In areas still affected, upgrading to a fully integrated formulation was necesary, as the slight increase in computational expense is outweighed by an improvement in response, as the results for V480P in figure 8 demonstrates. Capturing the localised stiffness is important for reinforcing members, so it is therefore recommended not to use under-integrated elements at these locations.

The floor construction can now be categorised and an assessment made in relation to their crashworthy response. Due to a variety of different frame types (continuous, double skinned, etc), as well as different joint sections (cross and t-type, etc), not all frames will be documented in this paper. Instead, a summary of the main features will be presented, highlighting areas of good and poor agreement. It should be remembered that only the port side could be considered, as the numerical idealisation did not take into account the predamage on the starboard side.

6.1 Continuous, single skinned frames

Frames V830, V480, V0, STN370A and STN1210A form the skeletal sub-structure, to which the eighteen load attachment points attach, with two pairs located at the front and aft of V480 and V830 and a pair along the mid point of V0. Figures 9, 10 and 11 provide a qualitative comparison between predicted and experimental deformations and a summary of their compacted heights at varying points can be found in tables 5, 6 and 7.

Due to the attached central load, frame V0 exhibits localised collapse, together with the buckling of the vertical stringers. The code predicts this failure mode, but overestimates the deformation due to the difference between measured and predicted heights shown in

table 5. No damage occurs along the aft and forward locations, due to the stiff intersection joints with STN370A and STN1210A respectively.

The behaviour for V480 port and starboard is in stark contrast to test, as the simulation predicts a single hinge line and collapse of both frames. In reality, deformation consists of upper hinge lines forming towards the aft of V480 in response to the failure of the upper seat rail and STN1210A, which causes this section of frame supporting the attached load. No deformation is observed at the forward sections, due to the strong intersection joints with STN370A.

Upon closer inspection of the numerical results, it was clear that the elements in the skin became separated from the water on account of nearby instabilities that develop, as shown in figures 10 and 11. This results in the adjacent water elements unexpectedly rising out of the surface of the water and providing an artificial buckling trigger for the frame. Once this occurs, the strength is drastically reduced, leading to an incorrect structural response. This artificial separation could be due to a number of factors, such as an inherent limitation with the code, or simply errors introduced as it is operating on its boundary of application. Equally plausible, this location could be predisposed to collapse due to geometrical modelling errors. As the same response was reported by As shown in figure 12, the same response was reported by DLR who used PAM-CRASH and their own coupled FE-SPH code, this which tends to suggest that modelling errors in the idealisation phase are a likely cause [16].

Tables 3 and 4 provide a comparison between test and simulation for the compacted heights of V480P and S, which are in good agreement towards the forward and aft

sections. The areas of poor agreement marked by an "*" should not be considered, as they coincide with element separation.

The overall damage for the midpoint of STN370A can be found in figure 13, which will be dealt with in two parts as its construction varies along its length. Between frames V480, STN370A is single framed, whereas between V480 and V830, the construction changes to a double skinned configuration, which will be dealt with in section 6.2.

For the single skinned frames, the skin deflections peak along the midpoint, with material failure occurring as the z-stringers cut into the surrounding frame (figure 13). The code is able to predict the location of the hinge lines, but underestimates the deformation, which may be attributed to the coarse element size assigned to the water.

6.2 Double skinned frames – effect of mesh sensitivity

Double skinned frames are located between V830 and V480 and result in a represent an increase in localised stiffness and a completely different failure mode, as shown in figure 14. Due to t The reinforced frame nature of this construction, this prevents the z-stringer from deflecting upwards and into the frame, so the localised material failure observed for the single STN370A does not occur. This reinforcing effect results in the failure of the weakest component first, which in this case are the rivets, which fail by tensile pull out. This results in causes a severe hinge line forming from the intersection with V480P, to the centre of this frame.

The numerical results demonstrate sensitivity to water element size. For a 5cm element length in figure 14b, the code predicts this hinge line, but the deformation is not severe

and there is no evidence of rivet failure. In figure 14c, the element size was reduced to 2cm, which captured the deformation more accurately, together with the associated frame separation and rivet failure.

The results clearly demonstrate the role of the water and the importance of ensuring the correct degree of loading is passed into the floor otherwise damage may be underestimated. Decreasing the element size enables a better transmission of water pressure, as the predicted damage converges to test. However, this is to the detriment of the run time, as the solution for the 2cm edge length component only prematurely terminated at ran to 8ms due to element instabilities caused the run to terminate, as opposed to 35ms for the 5cm case.

To conclude, the code is able to demonstrate convergence to test, but this comes at a high computational cost. There are no guarantees that a more detailed water component will provide a robust solution, due to the increased occurrence of instabilities seen in this research. Therefore, a trade off between predictive accuracy versus long-term stability will be required when developing a suitable water model.

6.3 Other frames

Frame STN1210A forms part of lower aft bulkhead and is a substantial component to which the port and starboard landing gear assemblies attach. A reinforcing rail also runs along its length and in addition to a variety of reinforcing brackets, results in a frame that is exceptionally strong. The frame retains its structural integrity and close numerical agreement is obtained, as damage is only observed around the base of the z-stringers., and localised frame collapse at the intersection with the transverse V-frames. This is

difficult to see from the orientation of the photograph in figure 15, but this behaviour is predicted by numerically.

7. Skin behaviour

The membrane behaviour of the skin is critical for an impact on water, as the Kinetic energy imparted to the water and the corresponding skin deflections shown in figures 5 and X 16, form a significant part of the energy absorbing process.

In order to assess the accuracy of the numerical results, deflection measurements were taken from the post impact floor, using horizontal and vertical datums from a fixed reference point taken at the intersection between V0 and STN1210A. The skin was divided into 9 zones and 51 Fifty one measurements were taken at evenly spaced intervals to coincide with the main V-frames, the z-stringers that marked the peak deflections, together with a set of measurements that lie between. Starboard deflections were not considered, due to the pre-damage already discussed.

Table 8 shows a comparison between the relative z-displacements for the skin at various port side locations, where a positive displacement means the point is higher than the reference point (i.e. it has moved inside the internal structure of the floor), and a negative value indicates the point is lower than the reference point. The locations are presented graphically in figures 17 through 19, which show clearly the location of the sampling points in relation to STN1210A, STN370A and the midpoint of the floor.

From the data presented, the trend for the displacements are in good agreement, but the code typically over and underestimates the deflections and the reasons for this will now

be discussed on a frame-by-frame basis. For all results presented, dynamic relaxation has not been taken into account.

STN1210A;

- Minimal skin deformation occurs, as the deflections observed for both test and simulation agree to within 1.5cm. are in close agreement and are of the order of 1.5cm relative to V0. The lack of deformation is caused by the strong nature of its construction and the stiff intersection joints with the transverse "V" frames.
- The results diverge at the intersection with V830P (Locations #22 and 25) and can be attributed to skin failure, which permits an increase in deflection and the large positive value observed experimentally. As no failure is predicted by the code, the simulation underestimates this deflection.

Midpoint between STN1210A and 370A;

- As shown in figure 18 for the mid section, the code consistently overestimates the deflections by approximately 3 to 4cm. Large discrepancies occur along V480P (locations #11, 14 and 17), which is caused by the artificial skin-water separation that has been discussed in section 6.1. The numerical results are capable of predicting the trend for the deflections, which infers that closer agreement could be obtained, provided the geometrical problems at this location can be resolved.

STN370A;

- For this frame, the trend and magnitude of the predicted displacements are in good agreement to test, as the code predicts the inward and outward deflections shown in figure 19. The code underestimates the deflections by an average of

1.5cm, but in locations where minimal deformation occurs, such as along the intersection joints, the predicted and observed deflections converge.

Considering the extremities of the floor, table 9 provides a comparison between the relative z-displacements for the skin at various locations for the port curved end section, which are presented graphically in figures 20 and 21.

The results are in good agreement, despite the deflections being consistently overestimated numerically. For example, the values for the lower part of the skin are approximately 1-2cm larger than reality, which is a small difference, especially when considering the distortion of the water elements at this location. It is clear from figure 20 that locations #30 and 36 are predicted to have a significant inward deflection either side of the lower reinforcing rail. However, this is a direct consequence of the formulation errors introduced into the solution and does not occur in reality.

Towards the upper rails to which the lift frames attach, the results presented in figure 21 are in close agreement to test (<0.5cm). The code consistently overestimates this deflection, but this is directly related to the movement of the lower skin and is of little concern.

The code has demonstrated an ability to predict with accuracy the trends and magnitudes of skin deflection to within a centimetre of test, which is extremely encouraging as dynamic relaxation has not been incorporated into the results. To conclude, the code is capable of distinguishing between true and artificial responses that are caused by numerical instabilities, providing increased confidence with this Lagrangian approach.

8. Time histories

After the drop test had been performed, it was found that the acceleration data was unavailable for comparison. , so could not be used for code validation [11]. In addition, the pressures time histories can be an extremely difficult parameter to measure experimentally, as cavitation effects can cause severe oscillations in the results. This is an extremely complex phenomenon that can cause problems for experimentalists, due to the problems of repeatability between successive tests [13].

In order to obtain comparable pressure histories, individual penalty-based surface-to-surface contact algorithms were defined at locations of interest. Only the slave side (skin) vertical force-time histories were recorded, which were divided by a representative area in order to determine the correpsonding pressures. The three locations presented in figures 22 through 24 represent different stiffness locations, corresponding to relatively "soft" areas that deflect quite significantly, such as the midpoint of V480S and the z-stringer between V480S and V0, and V0 itself, where very little deformation occurs.

High peak pressures were recorded underneath frames V480S (P3) and V0 (P7) in figures 22 and 24, of 179KPa and 253KPa respectively. The hard results are higher than those at the soft location, as a peak pressure of only 113KPa is recorded for the midpoint between V480S and V0 (P4) in figure 23. This is expected and can be explained by the differences in stiffness between the two locations, as the more deformable locations are better able to counteract the sudden increase in pressure by yielding plastically.

There appears to be no correlation to experiment, as the code predicts quite a varying response, ranging from an initial peak followed by the pressures reducing to zero, to a peak that is an order of magnitude larger than test. These extremes are a direct

consequence of the formulation used to represent the water, and a summary of the findings can be found below;

- Separation between water and structure – this leads to either a reduced pressure trace, or no time history at all, which raises questions as to the resolution of the mesh density assigned.
- If numerical instabilities develop and elements invert, this can introduce artificial contact forces resulting in pressure peaks with unrealistically large amplitudes.
- The penalty based contact algorithm is extremely susceptible to element size, as if contact is lost, pressure reduces to zero. It is not possible to guarantee that mesh refinements can overcome this limitation.

Another limitation of a Lagrangian approach is that it is not possible to recreate the interaction between structure-air-water and the corresponding dynamic impedance numerically with this technique. The compressibility of the boundary layer of air and the corresponding deflection of the water surface before the structure interacts may explain why the numerical pressures are higher than test. This raises the question as to whether the correct loading has been imparted into the structure, which is difficult to assess, due to the unreliability in obtaining consistent numerical traces.

To conclude, a Lagrangian approach has proven itself difficult to obtain reliable pressure histories and suggests that upgrading to an alternative formulation, such as ALE or SPH may be required. It would be interesting to see what effect this would have on the quality of the results, but this is beyond the scope of this present study.

9. Discussion

This section will provide an overview of the finite element approach adopted with a view for developing a methodology for fluid-structure interaction problems, together with identifying potential design improvements. This section will conclude with identifying potential areas of improvement that should be made in order to develop the water crashworthy characteristics of a typical metallic under floor design.

9.1 Finite element approach

The results presented in this paper were taken from a baseline simulation developed from sensitivity studies in order to provide a robust and computational inexpensive idealisation. The development of this finite element model encountered, many problems were encountered, which led to the development of recommended practises and techniques for modelling water using fixed mass elements. Many ideas have been discussed at length in this paper, so this section serves as a summary of the main findings;

- Element size, formulation and mesh density
- Solid element formulation
- Element instabilities
- Pressure-time histories
- Fully integrated elements are required for reinforcing components subject to large deformations in order to prevent hourglassing from affecting structural response.

- A closed continuous skin is essential in minimising element potential for instabilities developing in the water

Many problems were attributed to element size, where selection is heavily dependent upon the engineering judgement of the analyst and the level of detail required. This research has shown that refining the size can increase the level of predictive accuracy, but this comes at a cost of reducing the reliability of the solution. Decisions have to be made as to the level of fidelity required, as a purely Lagrangian approach has demonstrated its use in predicting a representative structural response. However, if a more detailed damage prediction analysis is required, upgrading to alternative formulations may be required.

The next major issue concerns the distorted water mesh, particularly at the boundary between fluid and structure, which is an inherent limitation using a fixed mass approach. Efforts need to focus upon minimising any geometric features that may promote instabilities. For example, the skin needs to be continuous with no open sections, as any discontinuities will introduce errors into the solution as the elements deform in an attempt to fill any developing voids, or will distort around any free surfaces as shown in figure 25.

In addition, the footprint of the impactor needs careful consideration as any perpendicular edges presented to the water will cause the elements to distort around any free surfaces, which is clearly demonstrated in figure 25 for the port landing gear. An assessment needs to be made as to the relevance of components like these in terms of transmission of load and its contribution to energy absorption, as engineering judgement may dictates the removal of a component to aid stability. , there is no guarantee this will eliminate this

problem. For example, removing the landing gear attachment did extend the simulation time, but mesh distortions eventually result in premature termination.

Concerning the pressure time histories, this is a difficult quantity to obtain, as it is based upon the penalty based contact algorithms. The quality of the results also comes into question, as a Lagrangian approach cannot recreate the layer of air and the actual dynamic impedance of test. This tends to suggest that the numerical pressures will be overestimated, which raises doubts over their use as qualification criteria for assessing the predictive accuracy of a simulation.

9.2 Limitations with the existing design

The quantitative and qualitative comparison between test and simulation has enabled limitations with the existing design to be identified, from a point of view of improving its crashworthiness on water. Two main areas have been identified, namely;

- Development of skin behaviour
- Degradation of stiff joint sections

The dominant mechanism for the transfer of water pressure is the deflection of skin between the longitudinal and lateral frames of the floor. In certain locations, this can be severe enough to result in material and / or rivet failure. This failure needs to be prevented at all costs as once this occurs, there will be no further transfer of the loading and the corresponding the ingress of water will cause secondary internal damage, together with reducing the floatation capabilities of the airframe. To increase the

membrane behaviour of the skin will require the use of composite materials, to which alternatives have already demonstrated their suitability for this application [17].

The second area for improvement concerns developing the intersection joints that form between longitudinal and lateral frames. This area of research is closely linked to the development of the skin, as successfully transferring the water pressure is essential if these joints and the attached frames are to collapse in a controlled manner.

Due to their construction, these joints are extremely strong and require high forces in order to initiate collapse. It has been demonstrated that the loads encountered during a water impact are significantly lower when compared to a hard surface impact, which means the collapse loads will not be reached and the stroke available is not fully utilised during a water impact [18].

In order to improve its crashworthy response, it is proposed that the next generation designs should encompass a passive dual role capability for hard and soft surface impacts, where the localised stiffness of the joints can be degraded, depending upon the type of surface encountered. Combining this dual role capability with an improvement in skin response will result in a vastly improved crashworthy structure and is an active area of research.

10. Concluding remarks

A Lagrangian approach to water modelling has been successfully developed to recreate the first 35 milliseconds of impact. Areas of good and poor agreement have been presented, which has allowed a characterisation of failure modes to this type of loading.

The numerical results have proved that the proposed approach may be used to capture the initial stages of a water impact, which for a crashworthiness analysis is where the most structural deformation occurs.

Accurately capturing the fluid response and the imparted loading is heavily dependant upon element size, as refining the mesh enables a more realistic water response, but at a cost of stability to the solution. Determining the right balance between element size and stability requires careful consideration of the model and engineering judgement.

Due to the penalty based nature of the contact algorithms, separation between water and skin elements is a common occurrence, which makes it difficult to obtain representative pressure time histories. Coupled with the fact that element and contact instabilities will also affect the traces obtained, means that the pressure results should not be used as a measure of the quality of the numerical results obtained.

This research has demonstrated two limitations with the existing metallic design. One area concerns the behaviour of the skin, as maximising its deflection without failure is critical to the transmission of the loading to other energy absorbing components. The second area for improvement concerns the intersection joints that are too strong from a water impact point of view. Having the ability to degrade their stiffness, depending upon the type of surface encountered will significantly improve the crashworthy response and safety of next generation metallic designs.

Acknowledgments

This work was performed within CAST, which is an acronym for "Crashworthiness of Helicopters on Water: Design of Structures Using Advanced Simulation Tools" and was funded by the European Community under the "Competitive and Sustainable Growth" programme (Contract G4RD-CT1999-0172).

REFERENCES

[1] Von Karman, Th. The impact of seaplane floats during landing, NACA Technical Note 321, October 1929

[2] Coltman, J.W., Neri, L.M., Analysis of US civil rotorcraft accidents for development of improved design criteria, National specialists meeting on crashworthy design of rotorcraft, American Helicopter Society, 1986

[3] Coltman, J.W., Domzalski, L., Arndt, S.M., Evaluation of the crash environment for US Navy helicopters……the hazards and Navy response, National specialists meeting on crashworthy design of rotorcraft, American Helicopter Society, Atlanta, Georgia, 1986

[4] Chen, C.C.T., Muller, M., Fogary, K.M., Rotorcraft ditchings and water related impacts that occurred from 1982 to 1989 – Phase I, US Department of Transportation, FAA Technical Center, Atlantic City, DOT/FAA/CT-92/13, October, 1993

[5] Muller, M., Rotorcraft ditchings and water related impacts that occurred from 1982 to 1989 – Phase II, US Department of Transportation, FAA Technical Center, Atlantic City, DOT/FAA/CT-92/14, October, 1993

[6] Fasanella, E.L., Jackson, K.E., Lyle, K.H., Finite element simulation of a full scale crash test of a composite helicopter, AHS 56th Annual Forum, Virginia, USA, 2000

[7] Wittlin, G., Smith, M., Sareen, A., Richards, M., Airframe water impact analysis using a combined MSC/DYTRAN – DRI/KRASH approach, AHS 53rd Annual Forum, Virginia Beach, Virginia, April 29- May 1, 1997

[8] Wittlin, G., Schultz, M., Smith, M.R., Rotary wing aircraft water impact test and analyses correlation, AHS 56th Annual Forum, Virginia, USA, May 2-4, 2000

[9] CAST – Crashworthiness of Helicopters onto Water – Design of Structures using Advanced Simulation Tools, funded by the European Community under the "Competitive and Sustainable Growth" programme (Contract G4RD-CT1999-0172), 2000-2003.

[10] CIRA – Centro Italiano Ricerche Aerospatziali, Italy. LISA Water impact facility.

[11] Vigliotti, A., "D3.2.5 Test report for sub structure No. 2", Task3.2/CIRA/3.2.5, Internal CAST report, May 2001

[12] Vigliotti, A., "D3.3.2 Instrument qualification report", Task3/CIRA/3.3.2, Internal CAST report, June 2001

[13] Anghileri, M., D5.5.1 Generic Water impact tests, Task 5.5/PM/V5.5.1, 20th October, 2001

[14] Hughes, K, Application of improved Lagrangian techniques for helicopter crashworthiness on water. *Phd Thesis*, Cranfield University, 2005

[15] Calvancanti, M.J., Vignjevic, R., A MSc/DYTRAN simulation of the lynx helicopter main lift frame collapse, MPhil Thesis, Cranfield University, 1996

[16] Pentecote, N., Vigliotti, A., Simulation of the impact on water of a sub floor component and a full-scale WG30 helicopter. *American Helicopter Society 58th Forum*, Montréal, Canada, June 11-13, 2002.

[17] Thuis, H.G.S.J., J de Vries, H.P.J., Wiggenraad, J.F.M. Sub-floor skin panels for improved crashworthiness of helicopters in case of water impact. American Helicopter Society 51st Forum, May 25-27, 1999

[18] Vignjevic, R., Meo, M., A new concept for a helicopter sub floor structure, crashworthy in impacts on water and rigid surfaces, International Journal of Crashworthiness, Volume 7, Issue 3, 2002

Figure Captions

Figure 1 Location of the component sub floors in relation to the main passenger section of the WG30

Figure 2 Test rig designed by CIRA for the $8ms^{-1}$ sub floor impact onto water, which shows the location of the ballast plates, together with the positions of the 18 seat rail attachment points [11]

Figure 3 Global view of the sub floor showing the location of the 18 attachment points that were constrained to alllow translation in the vertical direction only

Figure 4 Summary of the main locations of damage of the recovered sub floor

Figure 5 Deformation experienced along STN370A at the forward section of the sub floor

Figure 6 Underside view of the starboard landing gear assembly that shows the location of the replaced skin panel (white circle) and the missing landing gear attachment (red circle)

Figure 7 Evolution of damage and resulting water behaviour, 35ms after impact

Figure 8 The choice of element formulation can severely affect the resulting failure mode as the under integrated vertical stringers (a) and the fully integrated stringers (b) demonstrate

Figure 9 Comparison between the final states of deformation for frame V0

Figure 10 Separation that occurs due to an instability that develops in the water component on the reverse side of V480P shown in this figure

Figure 11 Comparison between the post impact and predicted states of deformation for V480 Sb

Figure 12 Similarities in the predicted collapse for V480P using a purely Lagrangian (a) and coupled FE-SPH (b) approach to water modelling. Both results were produced using PAM-CRASH by DLR [15]

Figure 13 Comparison between V480 port and starboard for frame STN370A

Figure 14 Comparison between LS-DYNA3D results and test for two element sizes for frame STN370A, located between V830S and V480S

Figure 15 Comparison between the post test component and the LS-DYNA3D predicted behaviour for the landing gear frame, STN1210A. As can be seen, very little deformation occurs

Figure 16 Underside view of the port side taken after the drop test. Picture courtesy of *CIRA* [11]

Figure 17 Comparisons between the relative skin deflections near STN1210A, located between V0 and V830P. All measurements taken relative to aft of V0

Figure 18 Comparisons between the relative skin deflections of the midpoint between STN1210A and 370A, located between V0 and V830P. All measurements taken relative to aft of V0

Figure 19 Comparisons between the relative skin deflections near STN370A, located between V0 and V830P. All measurements taken relative to aft of V0

Figure 20 Comparisons between relative skin deflections along lower part of port curved end section. All measurements taken relative to aft of V0

Figure 21 Comparisons between relative skin deflection along upper part of port curved end section. All measurements taken relative to V0

Figure 22 Comparisons between the pressure time histories for location 3 – V480S – 'Hard'

Figure 23 Comparison between the pressure time histories at location 4 – z-stringer between V480S and V0 – 'Soft'

Figure 24 Comparison between the pressure time histories at location 7 – V0 – 'Hard'

Figure 25 Deformation around port landing gear assembly at 5, 14.5 and 35ms

Tables

Item	Dimensions (length x height) (±0.001m)	Separation (m)
Longitudinal frames V0, V480 and V830	(0.950 x 0.143)	n/a
STN370A (transverse, single skin)	(1.655 x 0.144)	n/a
STN370A (transverse, double skin :V830-V480)	(0.474 x 0.144)	n/a
STN1210A (transverse)	(1.660 x 0.174)	n/a
Skin reinforcing z-section stringers	(0.960 x 0.311)	0.24
Rivet pitch	n/a	0.025

Table 1 Geometry of the major frame components

Component	Thickness (±0.01mm)
Outer skin	0.71
Continuous transverse frame (V830P to V830S)	1.20
Double transverse skin (V830 to V480) P and S	0.70
Longitudinal frame V0	1.20
Longitudinal frame V480 P / S	1.20
Z-stringers (attached to skin)	0.90
Longitudinal frame L-stringers	0.90
Fibrelam composite floor	10.0
Curved outer skin panels	0.90
Curved web (at STN370A)	1.90
Curved web (others)	0.70
Longitudinal frame STN1210A	1.50

Table 2 Thickness of the various components used in the construction of the floor

Item	Mass (±0.1kg)
Sub floor section	41.0
Impact trolley	338.4
Lead ballast	237.1
Mountings for sub floor	24.5
Extension cables	7.9
Total	**648.9**

Table 3 Distribution of mass for component sub floor

Effective Plastic Stress (MPa)	Effective Plastic Strain (%)
326.8	0.00
366.5	0.49
429.6	2.41
462.5	4.36
495.0	7.31
518.3	10.28
556.6	17.23

Table 4 Tabulated effective plastic stress vs. effective plastic strain for Al2014

Distance along frame (±0.1cm)		Experimental height (±0.1cm)	DYNA predicted height (±0.1cm)	% Difference (wrt. Exp)
0.0		15.2	14.7	-3.3 ±0.4
20.0		13.5	11.2	-17.04 ±0.09
40.0	*	11.8	9.1	-22.88 ±0.07
60.0		14.3	11.9	-16.78 ±0.08
80.0		15.2	15.2	0

Table 5 Comparison between experimental and DYNA predicted relative heights for frame V0

Distance along frame (±0.1cm)		Experimental height (±0.1cm)	DYNA predicted height (±0.1cm)	% Difference (wrt Exp)
0.0		14.8	14.4	-2.7 ±0.4
20.0		14.7	11.1	-24.49 ±0.06
40.0	*	14.6	8.8	-39.73 ±0.04
60.0		14.4	10.6	-26.39 ±0.05
80.0		13.8	13.6	-1 ±1

Table 6 Comparison between experimental and DYNA predicted heights for frame V480Sb

Distance along frame (±0.1cm)		Experimental height (±0.1cm)	DYNA predicted height (±0.1cm)	% Difference (wrt. Exp)
0.0		14.9	14.6	-2.0 ±0.6
20.0		14.7	11.0	-25.17 ±0.05
40.0	*	14.6	9.4	-35.62 ±0.04
60.0		13.8	11.5	-16.67 ±0.09
80.0		12.9	13.8	+7.0 ±0.2

Table 7 Comparison between experimental and DYNA predicted heights for frame V480Port

Location	X (±0.1cm)	Y (±0.1cm)	Relative Z Displacement Experiment (±0.1cm)	Relative Z Displacement LS-DYNA3D (±0.1cm)
1	0.0	8.0	0.0	0.1
2	0.0	48.0	-0.3	3.1
3	0.0	87.0	-0.8	0.7
4	12.0	8.0	1.3	1.5
5	12.0	48.0	2.5	5.7
6	12.0	87.0	1.5	1.5
7	24.0	8.0	1.1	1.4
8	24.0	48.0	3.0	5.9
9	24.0	87.0	3.5	2.1
10	36.0	8.0	1.3	1.3
11	36.0	48.0	1.2	5.9
12	36.0	87.0	0.5	0.1
13	48.0	8.0	-0.5	0.0
14	48.0	48.0	-1.8	4.4
15	48.0	87.0	-2.4	-1.5
16	56.5	8.0	0.5	0.0
17	56.5	48.0	0.8	4.9
18	56.5	87.0	-0.1	-0.9
19	65.0	8.0	0.2	0.1
20	65.0	48.0	2.0	3.9
21	65.0	87.0	0.6	-1.0
22	73.0	8.0	1.5	0.1
23	73.0	48.0	1.0	2.3
24	73.0	87.0	-0.1	-1.3
25	80.0	8.0	1.1	0.5
26	80.0	48.0	0.0	-0.1
27	80.0	87.0	-0.5	-1.9

Table 8 Comparison between the relative displacements of various points distributed across the skin, relative to a fixed reference point at the intersection of V0 and STN1210A

Location	X (±0.1cm)	Y (±0.1cm)	Relative Z Displacement Experiment (±0.1cm)	Relative Z Displacement LS-DYNA3D (±0.1cm)
28	-37.0	16.5	2.1	2.9
29	-37.0	0.0	15.2	14.5
30	-18.5	16.5	2.4	5.0
31	-18.5	0.0	15.2	14.9
32	0.0	16.5	2.8	4.3
33	0.0	0.0	15.5	15.1
34	10.0	16.5	3.0	4.7
35	10.0	0.0	15.5	15.1
36	20.0	16.5	3.3	5.3
37	20.0	0.0	15.6	15.1
38	30.0	16.5	3.5	4.3
39	30.0	0.0	15.6	15.1

Table 9 Comparison between experimental and LS-DYNA3D z displacements for the port end section, relative to aft of V0

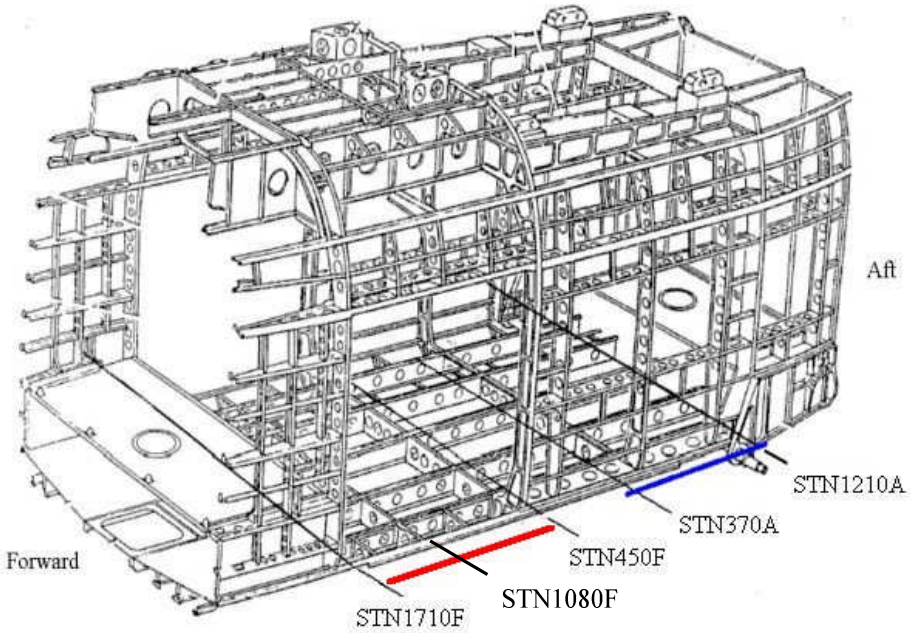

Figure 1 Location of the component sub floors in relation to the main passenger section of the WG30

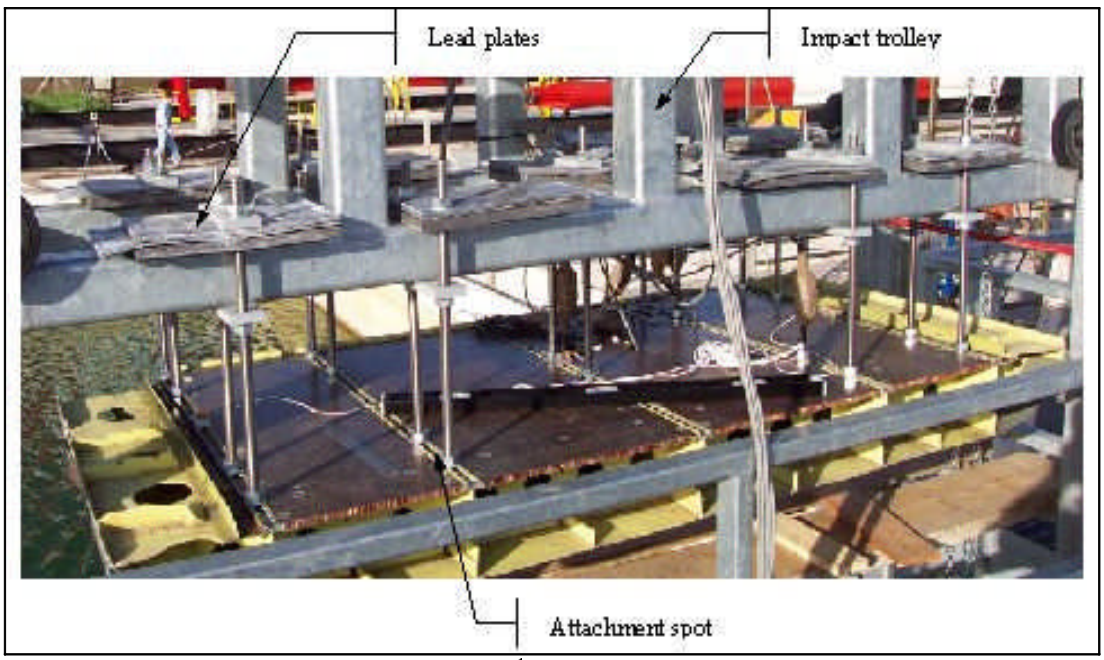

Figure 2 Test rig designed by CIRA for the 8ms^{-1} sub floor impact onto water, which shows the location of the ballast plates, together with the positions of the 18 seat rail attachment points [11]

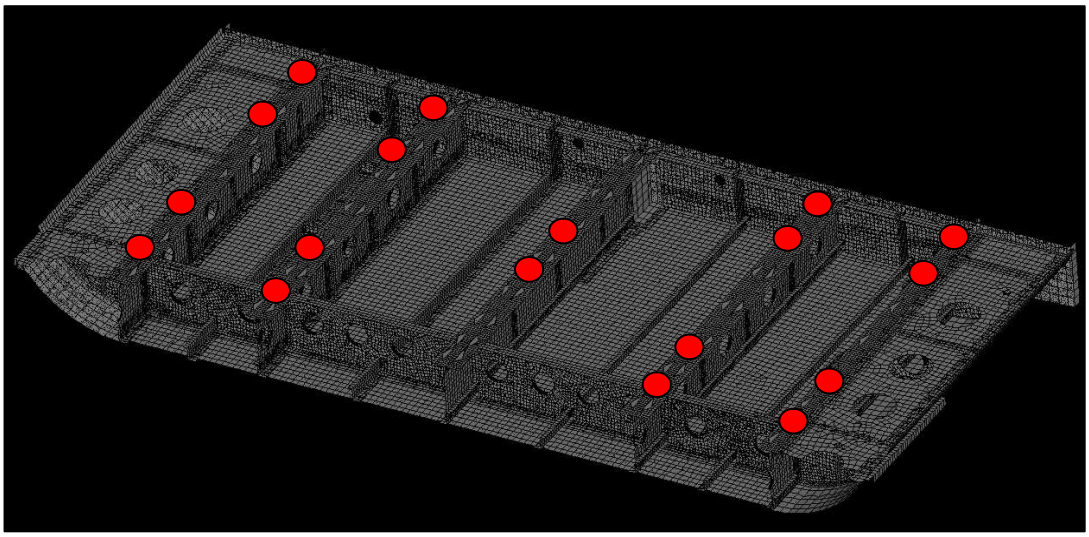

Figure 3 Global view of the sub floor showing the location of the 18 attachment points that were constrained to alllow translation in the vertical direction only

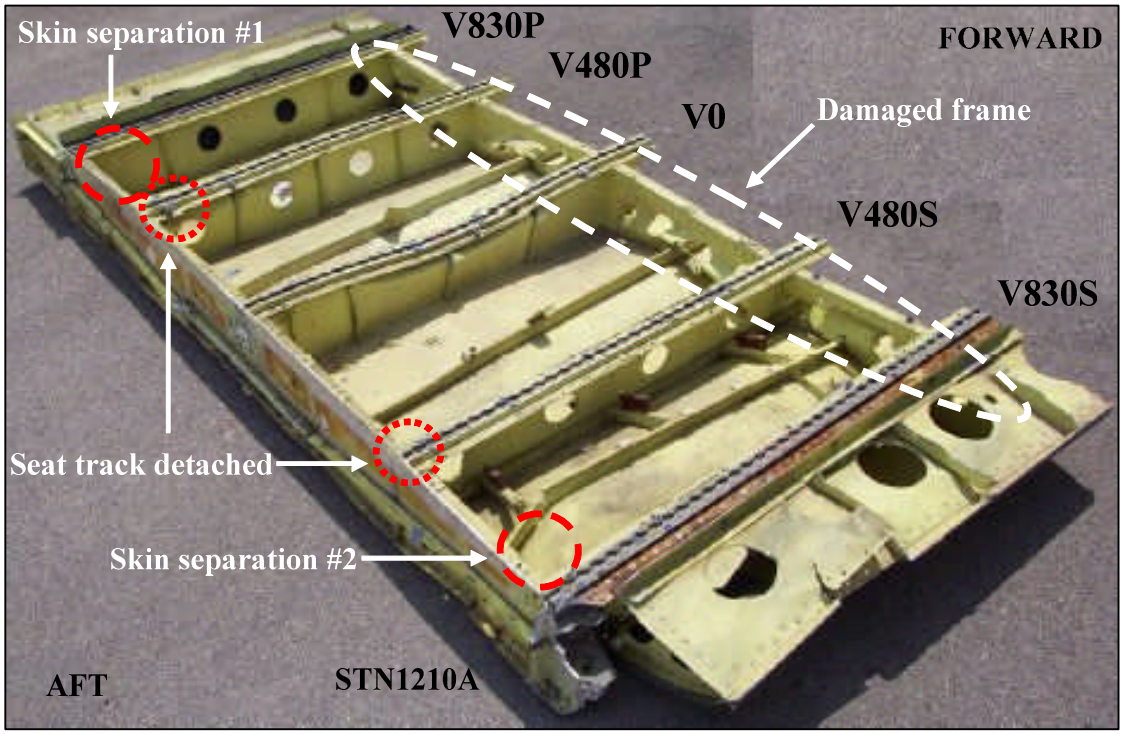

Figure 4 Summary of the main locations of damage of the recovered sub floor

Figure 5 Deformation experienced along STN370A at the forward section of the sub floor

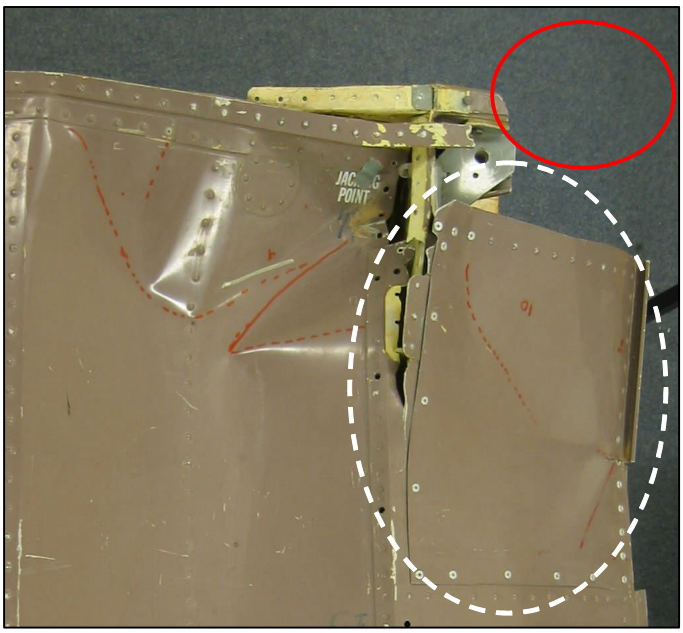

Figure 6 Underside view of the starboard landing gear assembly that shows the location of the replaced skin panel (white circle) and the missing landing gear attachment (red circle)

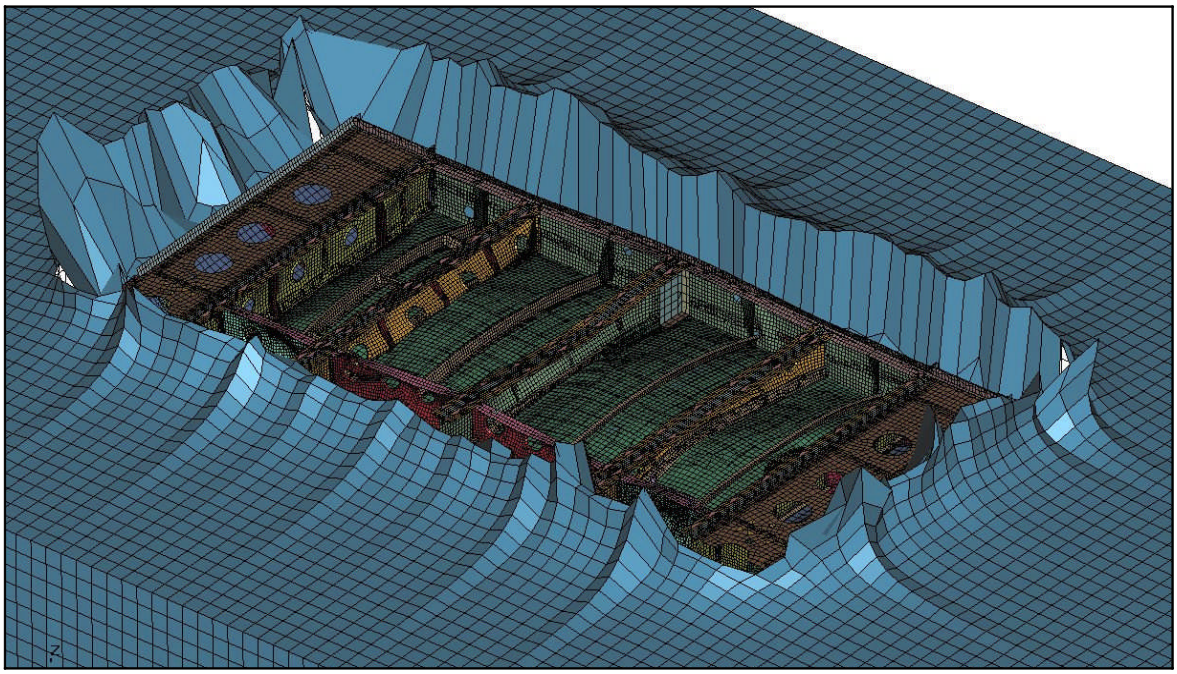

Figure 7 Evolution of damage and resulting water behaviour, 35ms after impact

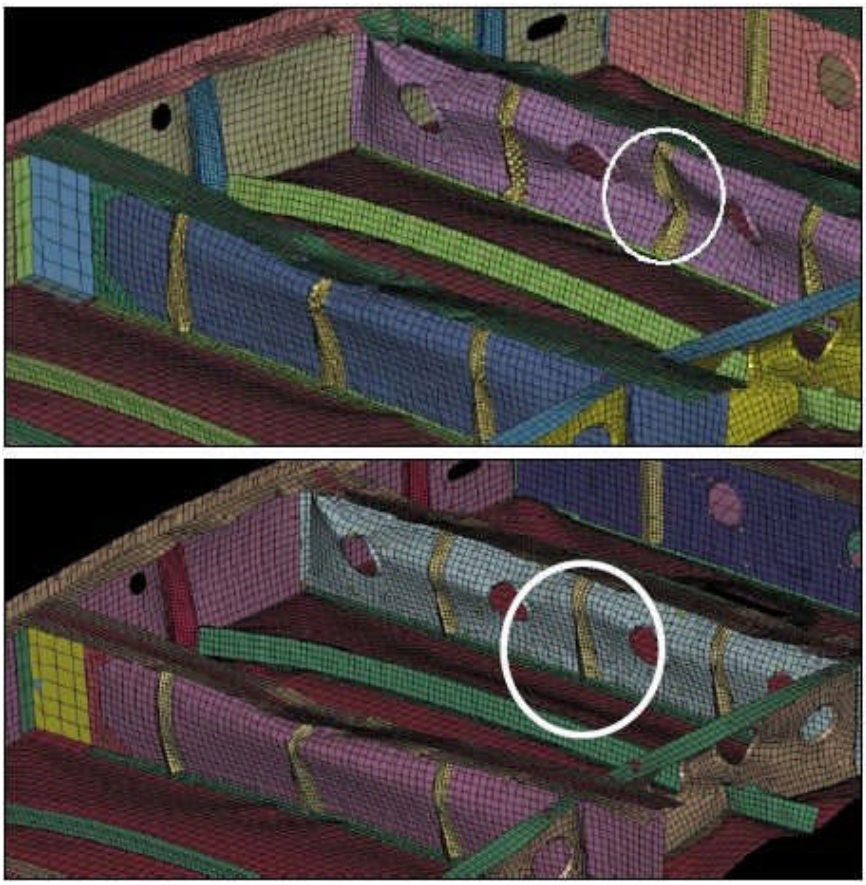

Figure 8 The choice of element formulation can severely affect the resulting failure mode as the under integrated vertical stringers (a) and the fully integrated stringers (b) demonstrate

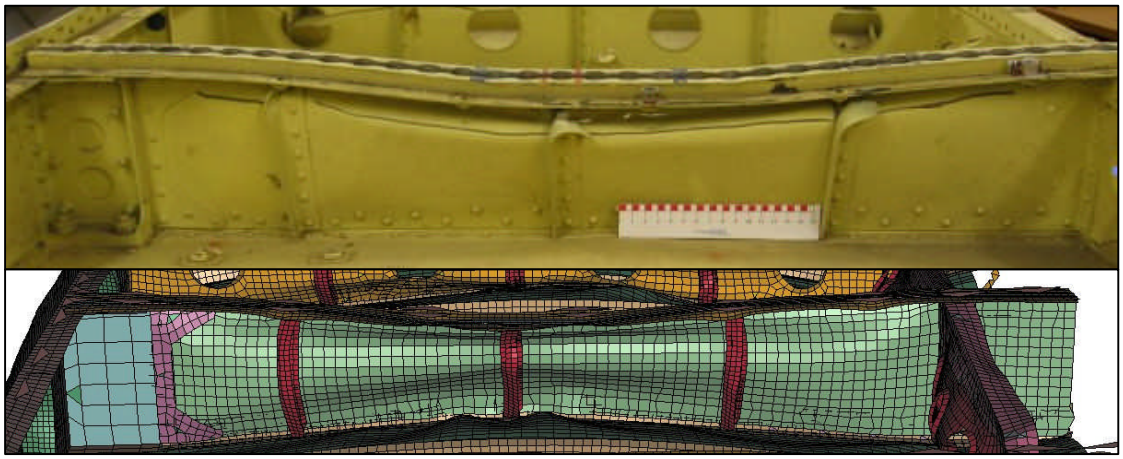

Figure 9 Comparison between the final states of deformation for frame V0

Figure 10 Separation that occurs due to an instability that develops in the water component on the reverse side of V480P shown in this figure

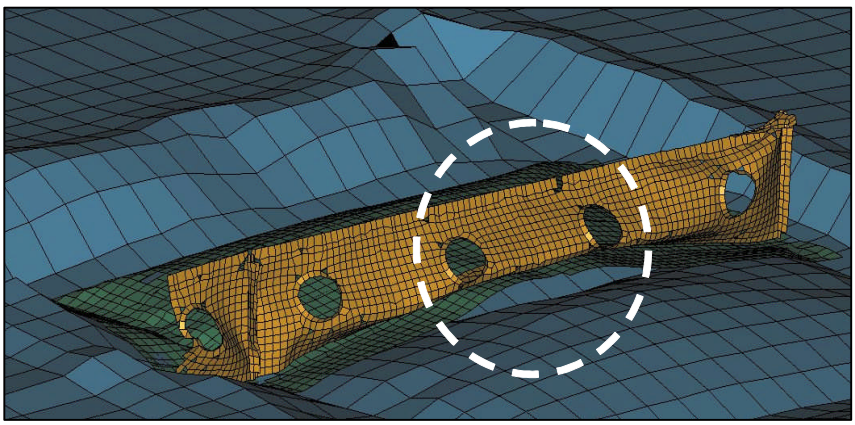

Figure 11 Comparison between the post impact and predicted states of deformation for V480 Sb

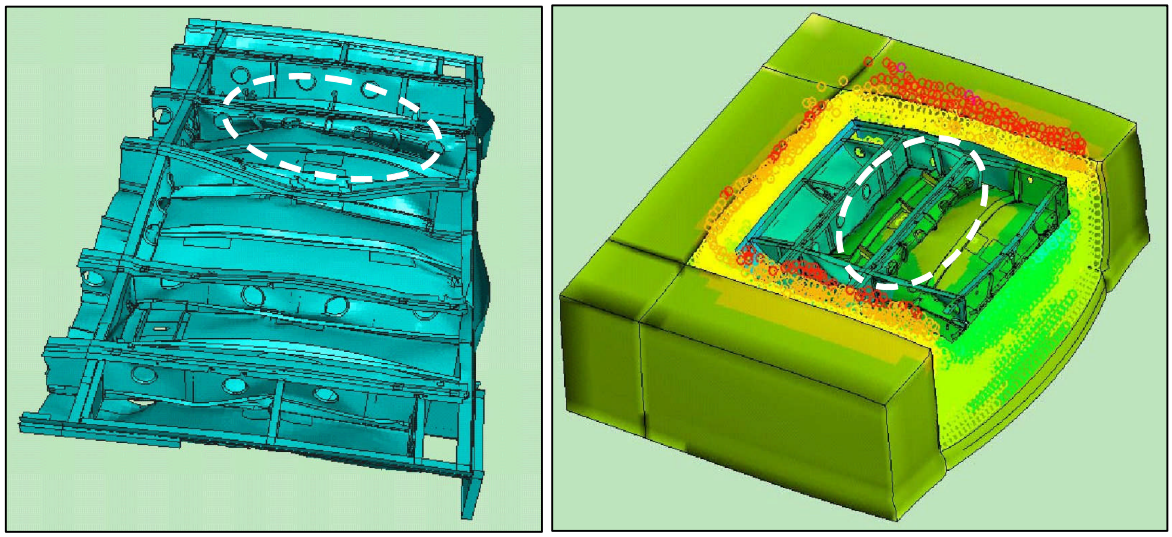

(a) Purely Lagrangian approach (b) Coupled FE-SPH approach

Figure 12 Similarities in the predicted collapse for V480P using a purely Lagrangian (a) and coupled FE-SPH (b) approach to water modelling. Both results were produced using PAM-CRASH by DLR [16]

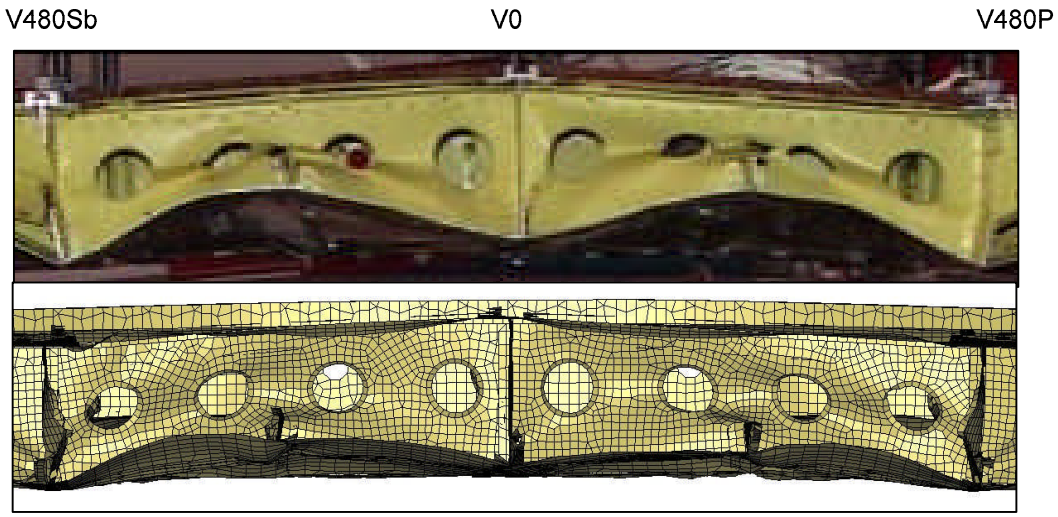

Figure 13 Comparison between V480 port and starboard for frame STN370A

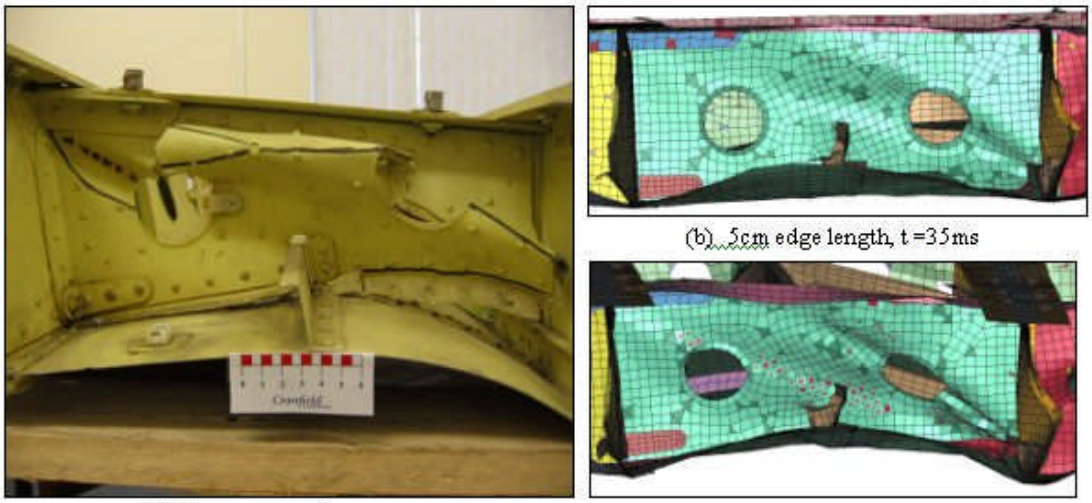

Figure 14 Comparison between LS-DYNA3D results and test for two element sizes for frame STN370A, located between V830S and V480S

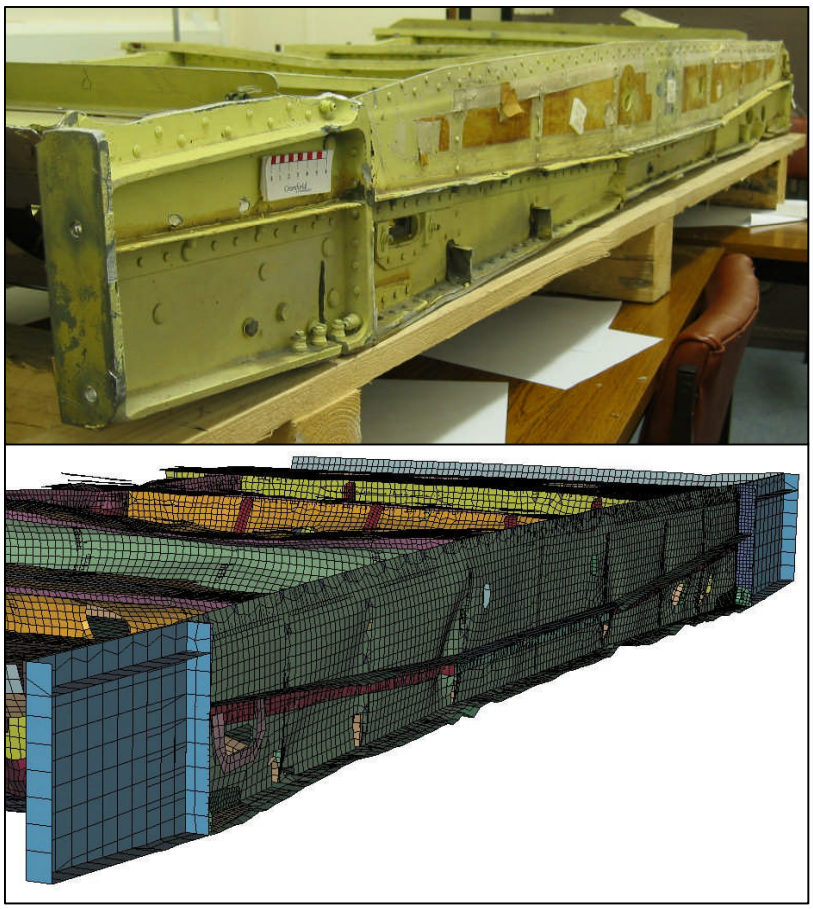

Figure 15 Comparison between the post test component and the LS-DYNA3D predicted behaviour for the landing gear frame, STN1210A. As can be seen, very little deformation occurs

Figure 16 Underside view of the port side taken after the drop test. Picture courtesy of *CIRA* [11]

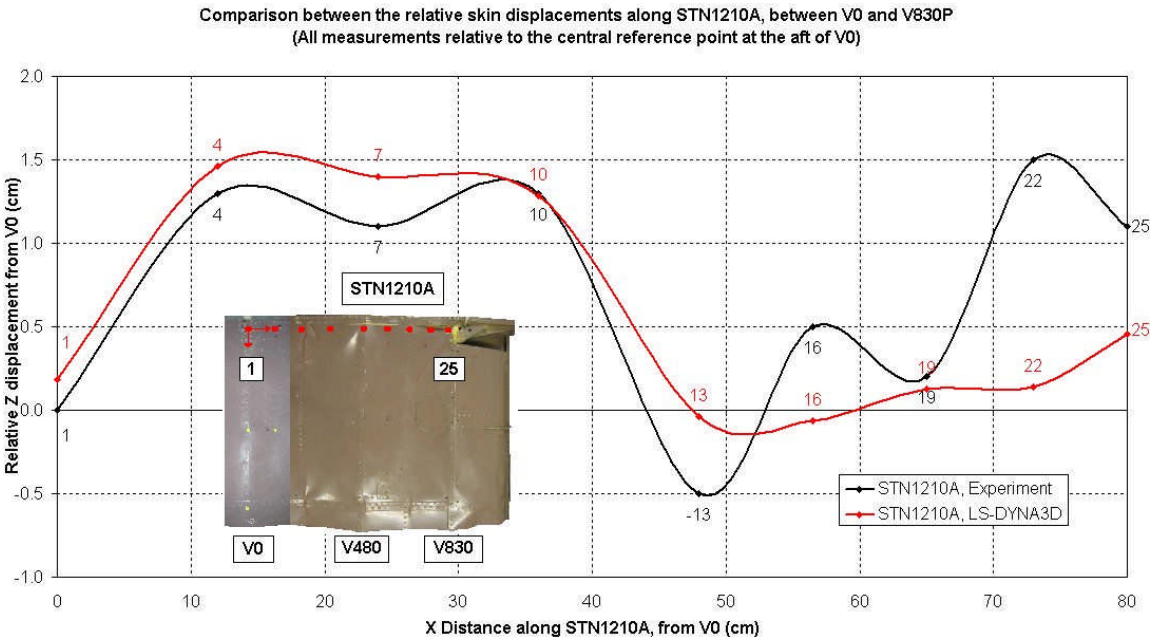

Figure 17 Comparisons between the relative skin deflections near STN1210A, located between V0 and V830P. All measurements taken relative to aft of V0

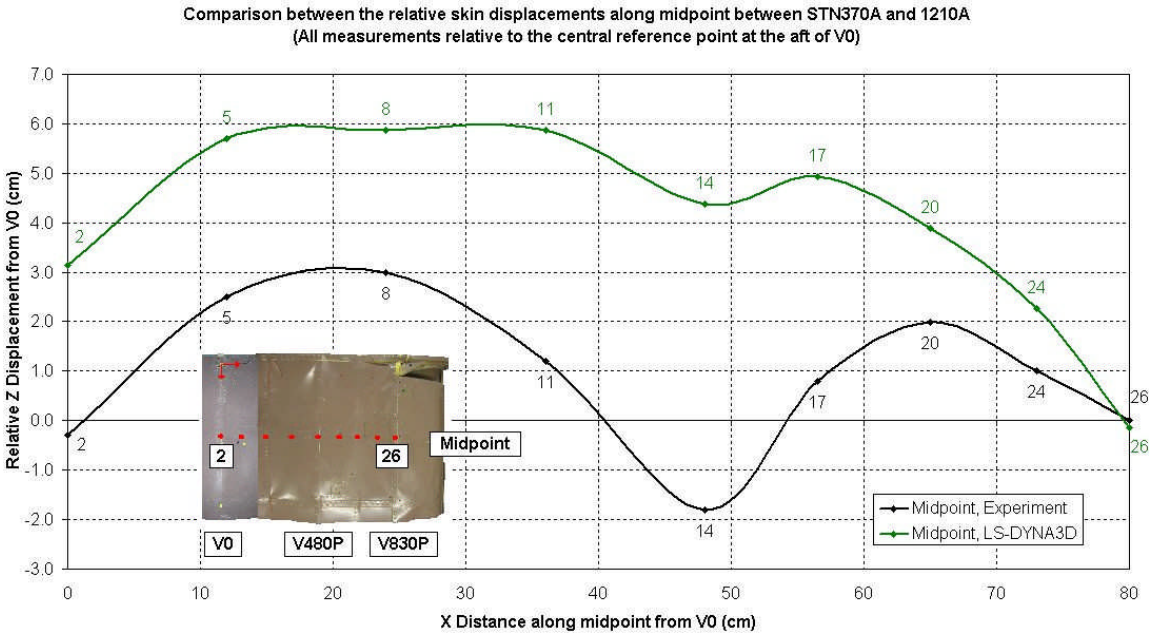

Figure 18 Comparisons between the relative skin deflections of the midpoint between STN1210A and 370A, located between V0 and V830P. All measurements taken relative to aft of V0

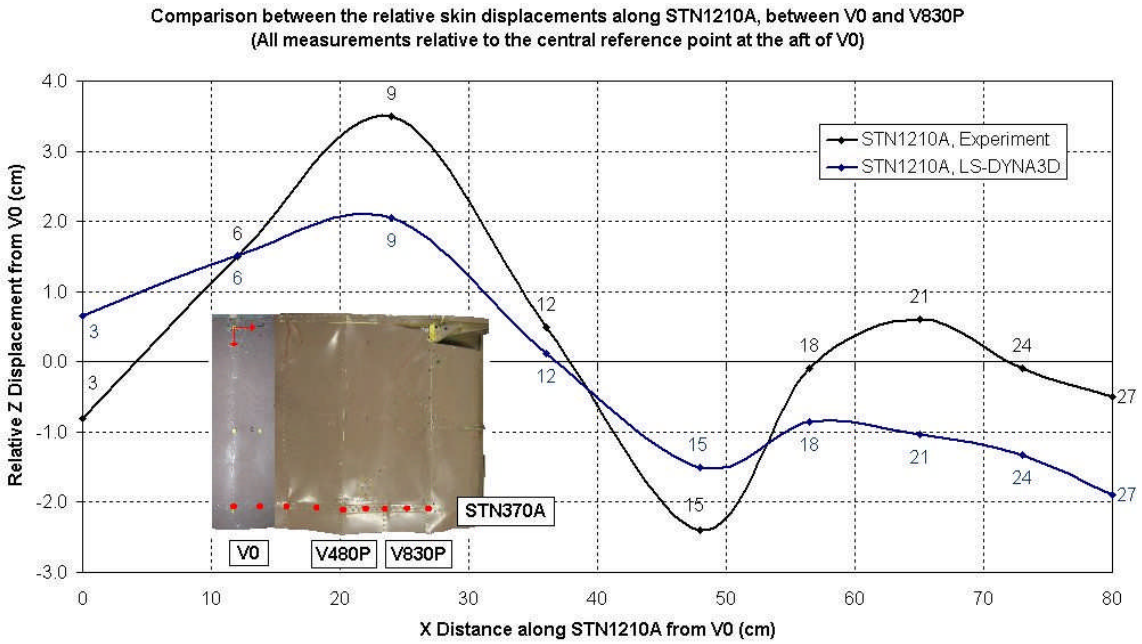

Figure 19 Comparisons between the relative skin deflections near STN370A, located between V0 and V830P. All measurements taken relative to aft of V0

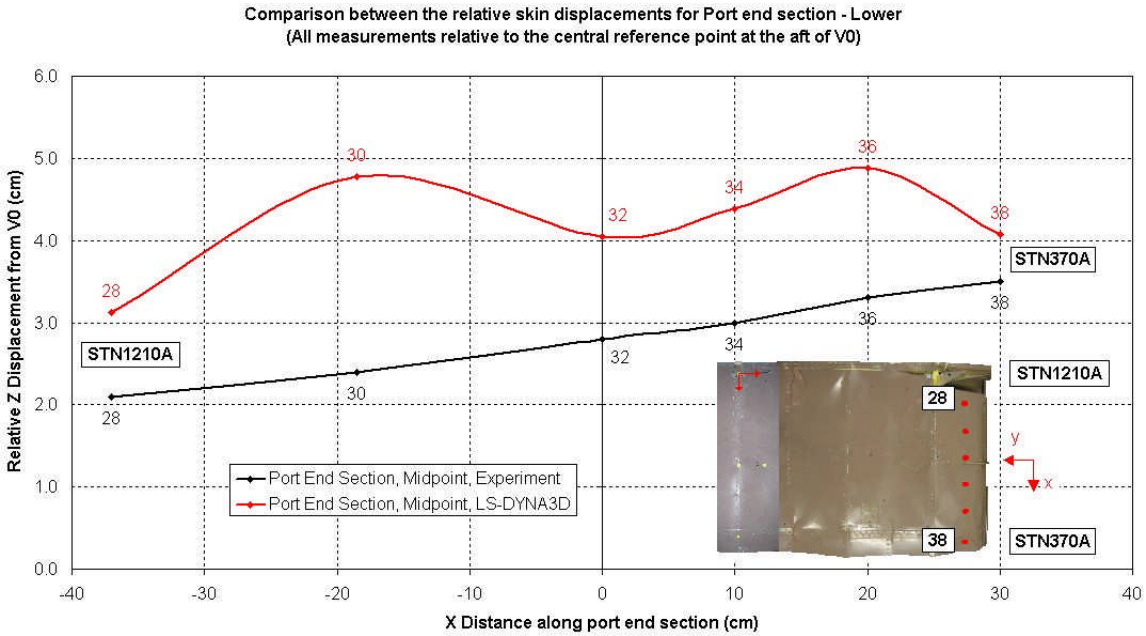

Figure 20 Comparisons between relative skin deflections along lower part of port curved end section. All measurements taken relative to aft of V0

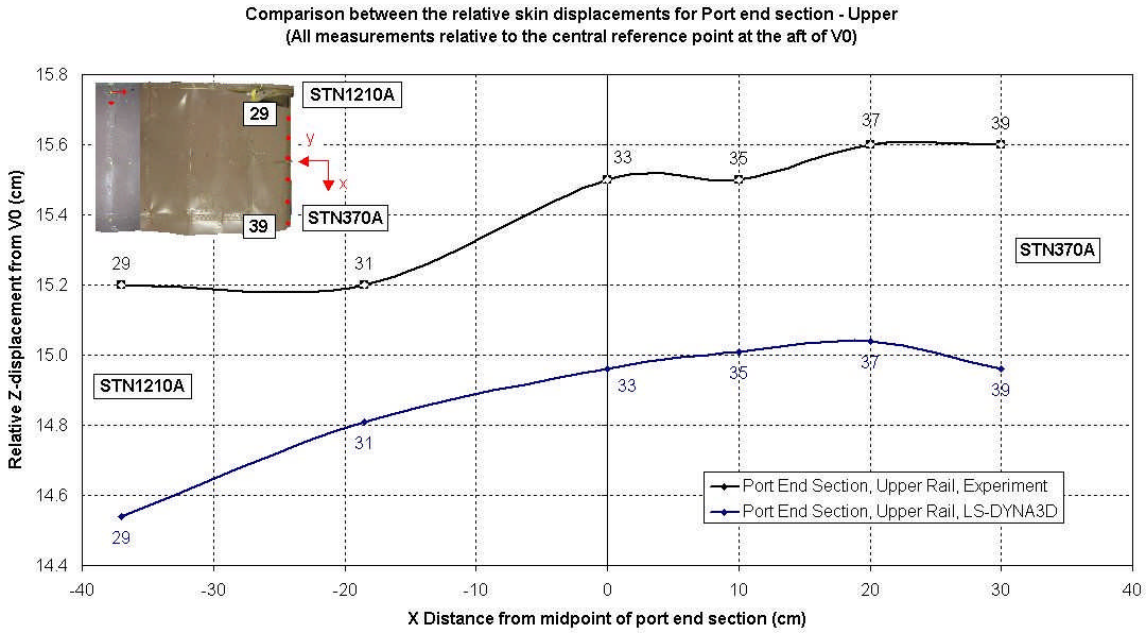

Figure 21 Comparisons between relative skin deflection along upper part of port curved end section. All measurements taken relative to V0

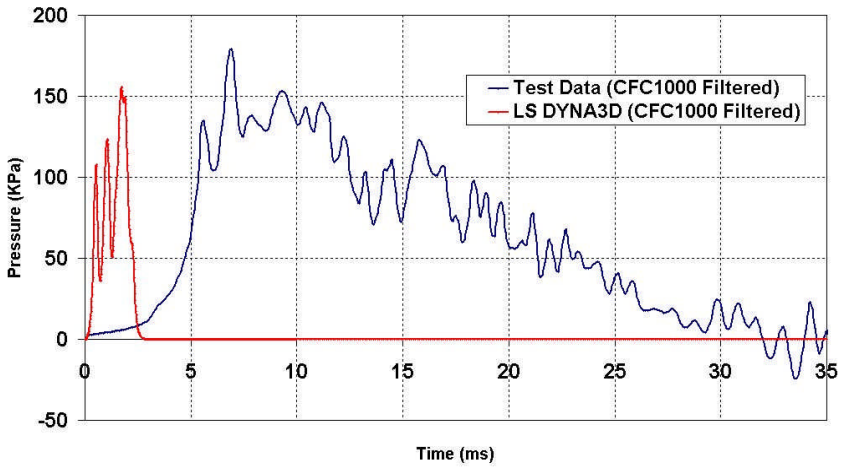

Figure 22 Comparisons between the pressure time histories for location 3 – V480S – 'Hard'

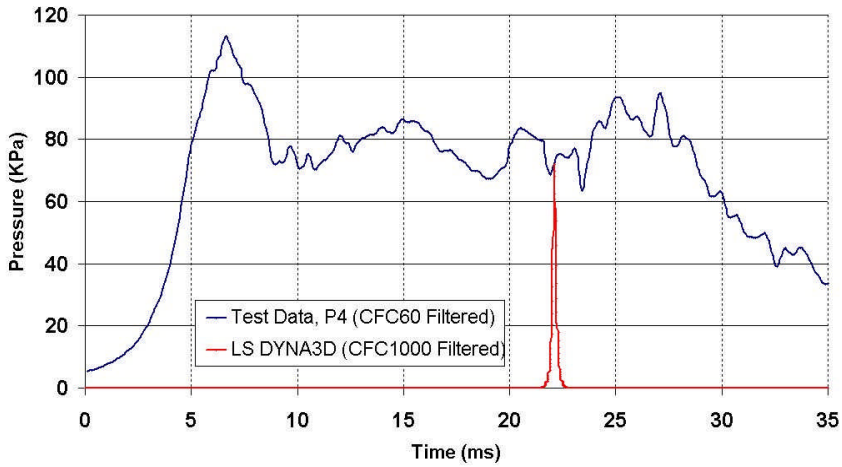

Figure 23 Comparison between the pressure time histories at location 4 – z-stringer between V480S and V0 – 'Soft'

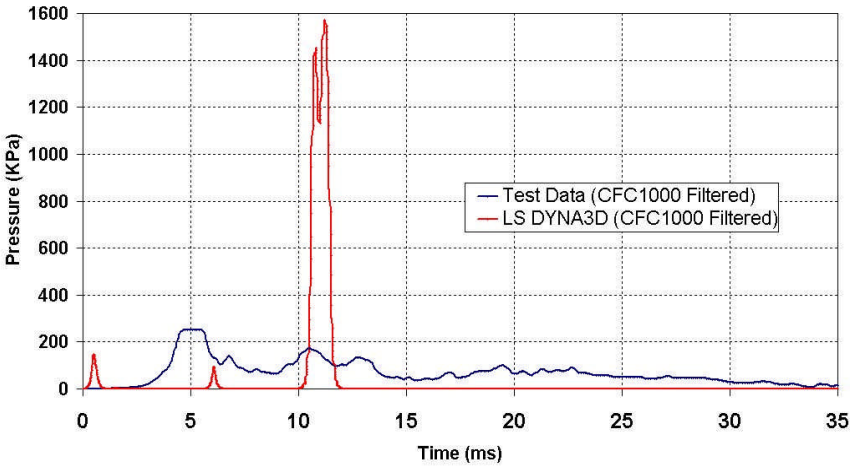

Figure 24 Comparison between the pressure time histories at location 7 – V0 – 'Hard'

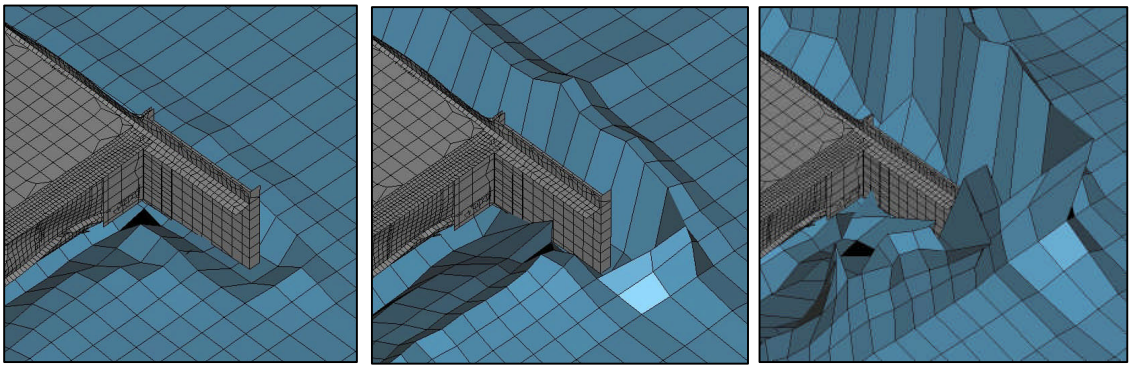

Figure 25 Deformation around port landing gear assembly at 5, 14.5 and 35ms